Modelling and
Simulation in Materials
Science and
Engineering

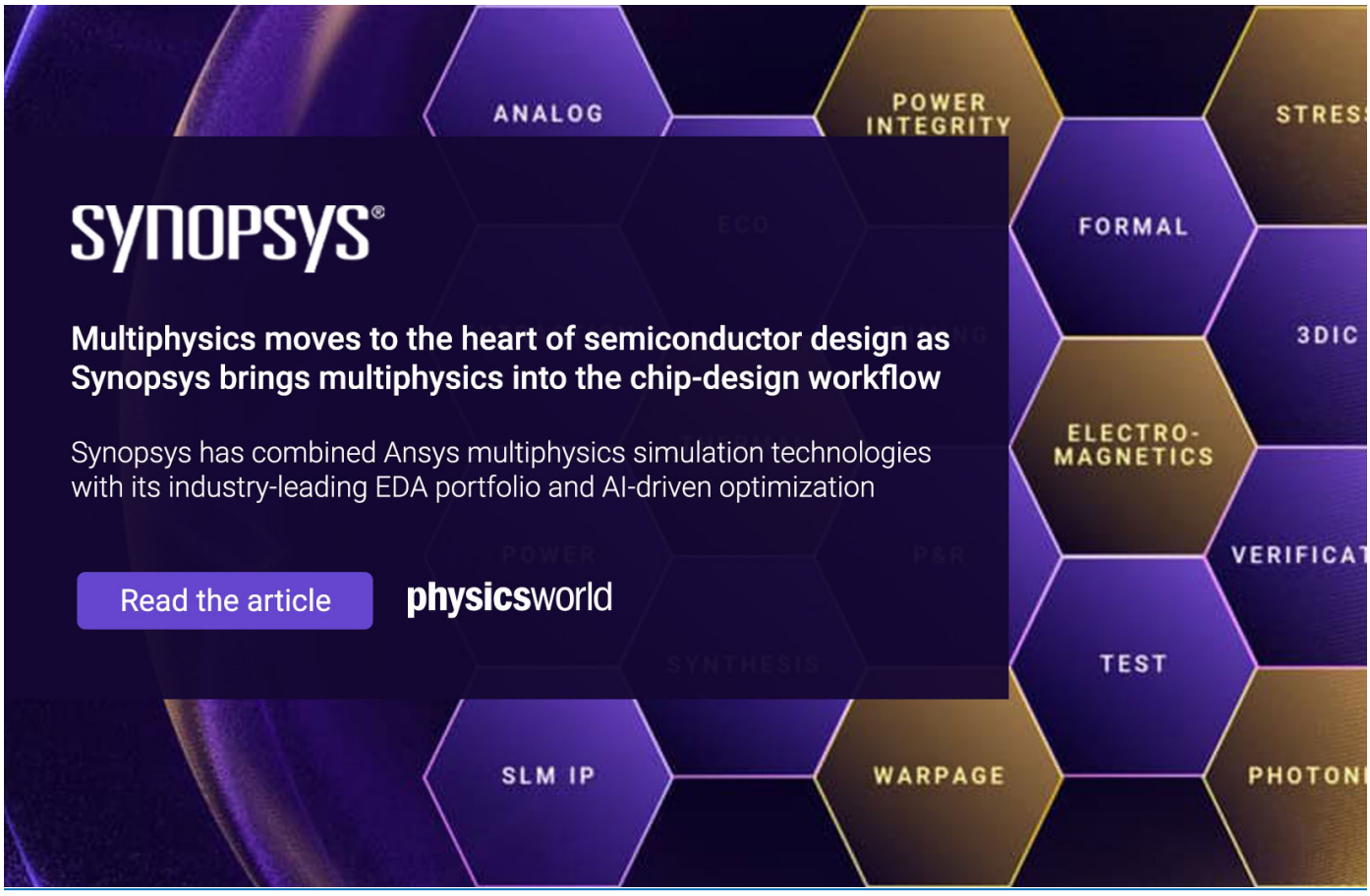
PURPOSE-LED
PUBLISHING™

PAPER

Modelling oxidation kinetics of half-Heusler thermoelectric materials and the role of protective coatings

To cite this article: Ekrem Ekici and Mikdat Gurtaran 2026 *Modelling Simul. Mater. Sci. Eng.* **34** 085001

View the article online for updates and enhancements.



Modelling and Simulation in Materials Science and Engineering

Check for updates

PAPER

RECEIVED
13 May 2026

REVISED
13 October 2026

ACCEPTED FOR PUBLICATION
26 October 2026

PUBLISHED
4 November 2026

Modelling oxidation kinetics of half-Heusler thermoelectric materials and the role of protective coatings

Ekrem Ekici[1,2] **and Mikdat Gurtaran**[3,4,*]

[1] Interdisciplinary Research Center for Biosystems and Machines, King Fahd University of Petroleum and Minerals, Dhahran, Saudi Arabia
[2] Department of Mechanical Engineering, Bogazici University, İstanbul, Türkiye
[3] Interdisciplinary Research Center for Advanced Materials, King Fahd University of Petroleum and Minerals, Dhahran, Saudi Arabia
[4] Department of Materials Science and Engineering, Izmir Institute of Technology, İzmir, Türkiye
[*] Author to whom any correspondence should be addressed.

E-mail: mikdat.gurtaran@kfupm.edu.sa

Keywords: finite element method, thermoelectric materials, oxidation kinetics, protective coating, diffusion

Abstract

Thermoelectric (TE) materials are increasingly utilised for electricity generation by harvesting waste heat in various practical applications. When deployed in high-temperature environments, their long-term thermal stability is crucial for ensuring high reliability and minimised mechanical degradation. While state-of-the-art experimental studies have highlighted the potential of half-Heusler TE materials in energy harvesting, experimental testing durations are often limited, leaving long-term performance uncertain. This paper addresses these gaps through finite element-based oxidation modelling, which explicitly accounts for the influence of protective coatings. Oxygen diffusion is modelled with a 1D Fick's equation solved with FEniCSx, with a time-decaying diffusivity in both the substrate and coating domains. The model is calibrated against 50 h mass-gain data for uncoated and CrSi-coated half-Heusler TE materials. With the calibrated parameters, the framework is used to extrapolate mass gain and oxide-scale growth, and can serve as a tool for estimating the long-term thermal stability of TE materials protected by oxidation-resistant coatings.

1. Introduction

Half-Heusler (HH) materials have attracted significant attention as promising candidates for thermoelectric (TE) applications, owing to their improved energy-conversion efficiency at medium to high temperatures [1–3]. Compounds such as MNiSn- and MCoSb-based systems (M = Hf, Zr, Ti) exhibit competitive TE performance and are considered strong candidates for practical energy-harvesting systems [4, 5], especial ly in automotive and industrial waste-heat recovery [6]. Despite these superior properties of HH materials, their long-term thermal stability under service conditions remains a critical challenge, limiting their large-scale deployment [7].

HH materials are prone to oxidation at high temperatures, leading to surface oxidation, elemental diffusion, and potential sublimation of volatile elements such as Sb and Sn [8, 9]. These degradation mechanisms alter the chemical composition, microstructure, and carrier transport properties of the material, ultimately reducing thermoelectric efficiency. In addition, the post-oxidation products might exhibit reduced mechanical stability, leading to degradation of the TE module over time [10, 11].

To address these issues, protective eco-friendly Si-doped Cr-based coatings have recently been applied to enhance the oxidation resistance and chemical stability of HH materials [12, 13]. While experimental studies contribute to understanding the oxidation behaviour of TE materials and protective coatings, it is crucial to predict the long-term thermal stability of the material/coating to design reliable TE modules. In addition, predictive modelling enables quantitative description of oxidation rates, kinetics, and diffusion-controlled processes over long operating durations, which is particularly valuable for material selection, coating design, and system-level integration in TE technologies.

© 2026 IOP Publishing Ltd. All rights, including for text and data mining, AI training, and similar technologies, are reserved.

Oxidation in materials is often modelled using a linear rate law, a cubic rate law, a parabolic rate law, or a logarithmic rate law [14]. These models usually include parameters such as diffusion rate and oxidation time. Considering anion and cation diffusion in the metals, Wagner first introduced a theory for oxidation to model oxide scale formation [15], and it has been extended to cover alloys [16]. Typically, oxidation models consider two distinct domains: one for the designated oxide layer and the other for the oxidised substrate. The oxidation kinetics for the former are modelled with a parabolically decaying diffusion coefficient that follows the Arrhenius law, to include temperature effects analytically. Further, numerous oxidation studies are available for titanium using the Arrhenius law [17, 18], and a finite-volume method scheme is introduced for modelling oxide-scale formation and total mass gain in α and near-α titanium alloys [19, 20]. For the numerical modelling of the chemical evolution of oxygen in Ni-base alloys, a finite-volume-based solver, EKINOX, was introduced in [21]. This code is then gradually extended to modelling the oxidation kinetics of zirconium alloys (EKINOX-Zr) [22] and Ni-Cr alloys [23], considering the effect of moving interfaces. Following these, a numerical tool called PyTiOx is introduced by Ciszak *et al* For modelling moving oxide-metal interfaces to obtain quantitative effects of Ti6242s alloy oxidation by also giving life span estimations [24]. These studies show that diffusion-based models can reproduce the oxidation kinetics of metallic alloys. For half-Heusler TE materials, however, oxidation has been studied only experimentally so far, and no numerical oxidation model has been reported. Classical rate laws fitted to mass-gain data give a rate constant but not the oxygen distribution in the material. Therefore, they cannot represent a coated substrate or predict the effect of coating thickness. Furthermore, long-term performance modelling for protective coatings on TE materials remains undeveloped-a critical gap that must be addressed for practical industrial applications.

In this paper, motivated by the shortcomings in TE material modelling identified above, the oxidation behaviour of N-type and P-type complex-structured HH materials is numerically investigated for the first time using finite element-based oxygen diffusion modelling. In addition, the thermal behaviour response of the CrSi protective coating at 500 °C was modelled. A detailed numerical discretisation is described, and decaying diffusion coefficients for both the TE material and the protective coating are introduced and characterised by three parameters: the initial diffusion coefficient, the decay rate, and the oxygen molar mass fraction. Using these three characteristic parameters for N-type and P-type TE materials and CrSi coating, experimental oxidation cases in [7, 12] are modelled for 50 h with the proposed numerical framework. Furthermore, these calibrated material parameters are used to determine the long-term oxidation behaviour of TE materials and protective coatings, which are to be investigated through parametric numerical extrapolation studies. To assess the effectiveness of the protective coating, the thickness of the oxide scale after 1000 h of oxidation was predicted, and the impact of coating thickness on mass gain was modelled. By combining calibration and extrapolation test cases, this study paves the way to determine the oxidation performance of TE materials and to design effective oxidation-protective coatings to ensure long-term thermal stability.

2. Oxidation modelling

This section presents the implemented finite element framework to solve Fick's equation to model oxidation. The discretisation and weak formulations are given. Next, the explanation of the time-decaying oxygen diffusivity distribution is provided, and the boundary conditions (BCs) and mass gain calculation procedure are described.

2.1. Fick's equation for oxygen diffusion

For modelling the oxidation in TE materials, the diffusion equation that follows Fick's second law to model the oxygen diffusion over the numerical domain is solved [14]:

$$\frac{\partial c}{\partial t} = D\left[\nabla \cdot \nabla c\right] \quad \text{in } \Omega, \tag{1}$$

where c is the normalised (between 0.0 and 1.0) diffused oxygen, t is the time and D is the diffusion coefficient for the domain Ω.

2.2. Discretisation and weak formulation

A finite element method (FEM) scheme is used to obtain oxygen concentration mobility on the spatial material domain. Therefore, a discretisation in time and space is needed for the Fick's system (1) and its

BCs. For the time level n, (1) can be written as:

$$\left(\frac{\partial c}{\partial t}\right)^{n+1} = D\nabla^2 c^{n+1}. \tag{2}$$

For approximating the partial time derivatives, finite differences is imposed to approximate the left-hand side of (2):

$$\left(\frac{\partial c}{\partial t}\right)^{n+1} \approx \frac{c^{n+1} - c^n}{\Delta t}, \tag{3}$$

where Δt is the time step. For the time level $t = n + 1$, implicit Euler discretisation is chosen to obtain:

$$\frac{c^{n+1} - c^n}{\Delta t} = D\nabla^2 c^{n+1}. \tag{4}$$

At this stage, the terms in (4) can be multiplied with test function v and the resulting terms can be integrated over the numerical material domain Ω:

$$\int_\Omega \frac{c^{n+1} - c^n}{\Delta t} v \,\mathrm{d}\,\mathrm{x} = \int_\Omega D\nabla^2 c^{n+1} v \,\mathrm{d}\,\mathrm{x}. \tag{5}$$

Further substitution of c^{n+1} with c and integration of the second order terms in (5) by parts (to reduce the derivative order of c) gives:

$$\int_\Omega \frac{c^{n+1} - c^n}{\Delta t} v \,\mathrm{d}x = -\int_\Omega D\nabla c^{n+1} \cdot \nabla v \,\mathrm{d}x + \int_{\partial\Omega} D\left(\nabla c^{n+1} \cdot \mathbf{n}\right) v \,\mathrm{d}s, \tag{6}$$

where the boundary integral vanishes on $\partial\Omega_\mathrm{D}$, where $v = 0$, and on $\partial\Omega_N$, where $g = 0$. Finally, terms in (6) can be rearranged to obtain bilinear finite element system, $a(c, v) = L(v)$, where the left hand side reads

$$a(c, v) = \int c\ v\ \mathrm{d}x + \int \Delta t D\ \nabla c \cdot \nabla v\ \mathrm{d}x, \tag{7}$$

and the right-hand side reads

$$L(v) = \int c^n\ v\ \mathrm{d}x. \tag{8}$$

Noting that the del operator $\nabla = \frac{\partial}{\partial x}\mathbf{i} + \frac{\partial}{\partial y}\mathbf{j} + \frac{\partial}{\partial z}\mathbf{k}$ is for Cartesian grid with corresponding unit vectors. To solve the finite element system, the open-source FEM framework, FEniCSx project [25] is used, which provides subroutines for solving finite element systems. Initially, the derived weak form (6) is defined using the high-level unified form language (UFL) [26] using its Python interface. Then, the FEniCSx Form Compiler (FFCx) [27] handles these UFL definitions, and DOLFINx then uses these to assemble the global sparse matrix system. This system is further solved using the portable extensible toolkit for scientific computation (PETSc) [28] via its Python binding, petsc4py [29]. An analytical verification test case for the implemented diffusion solver is given in appendix A.

2.3. Diffusivity coefficient

To capture the parabolic oxidation behaviour of both the substrate and coating materials, domain-specific diffusion coefficients are used to model the decrease in mass gain over time. Coating materials exhibit significantly higher oxidation resistance than the substrate [30], leading to distinct diffusion kinetics between the two domains. Given that TE materials typically exhibit parabolic oxidation profiles, the model employs a diffusivity field that decays according to a specific parabolic rate. For representing this numerically, a diffusion coefficient to decay over time may be introduced:

$$D = D_0 \mathrm{e}^{-k \cdot t}, \tag{9}$$

where D_0 is the initial diffusion coefficient at $t = 0$ and k is the decay rate of the D_0. For the uncoated TE material case (purely substrate), the initial diffusivity coefficient ($D_{0,s}$) and decay rate (k_s) purely depend on the substrate material, whereas the coated TE materials possess additional diffusivity parameters (D_c, k_c) to represent the oxidation behaviour of the coated surface being subjected to high temperature oxidation. With calibrated diffusion parameters for both domains, a more accurate representation

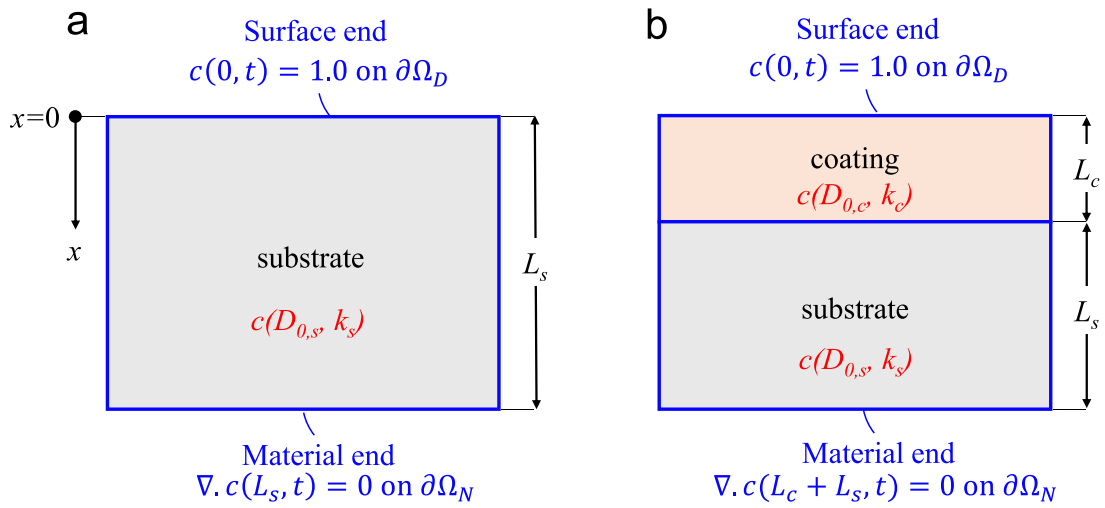


Figure 1. One-dimensional boundary conditions for (a) uncoated and (b) coated cases with corresponding geometrical and diffusion parameters.

of the multi-material oxidation kinetics may be achieved. In some studies, a similar approach is adopted by using two different calculation media for the oxide scale and the substrate [24]. The schematic representations of both cases, along with the corresponding diffusion and geometry parameters, are shown in figure 1.

2.4. BCs

Fick's equation (1) is second order in space. In one dimension, it requires one BC at each end of the domain. The two ends represent different physical situations. Therefore, two types of BCs are used.

At the exposed surface, the material is in contact with the oxidising atmosphere, which acts as a constant oxygen supply. The normalised oxygen content is prescribed on this boundary, $\partial\Omega_{\mathrm{D}}$, with a Dirichlet BC:

$$c = c_{\mathrm{D}} \quad \text{on } \partial\Omega_{\mathrm{D}}, \tag{10}$$

where c_{D} is the specified normalised oxygen content. At the inner end of the substrate, the oxygen content is not known in advance, but the oxygen flux is. The flux is prescribed on this boundary, $\partial\Omega_{\mathrm{N}}$, with a Neumann BC:

$$D\nabla c \cdot \mathbf{n} = g \quad \text{on } \partial\Omega_{\mathrm{N}}, \tag{11}$$

where $\mathbf{n}$ is the outward unit normal and g is the specified normalised oxygen flux. If $g = 0$, the boundary is impermeable and no oxygen crosses it.

In the finite element setting, the Dirichlet BC is called essential, because it is imposed explicitly on the solution space and the test function vanishes on $\partial\Omega_{\mathrm{D}}$. The Neumann BC is called natural, because it enters through the boundary integral of the weak form (6). For $g = 0$, this integral vanishes and the condition is satisfied without further treatment.

The numerical setup for the 1D case is implemented with a Dirichlet BC on the surface end, $c_{\mathrm{D}}(0,t) = 1.0$, and zero Neumann BCs at the material end, $D\nabla \cdot c(L,t) \cdot \mathbf{n} = 0.0$. The selection of Neumann BC for the material end is deliberate, as the diffusion front takes a considerably long time to reach there for a chosen total length (section 2.6), and that boundary can then be assumed to be impermeable. The 1D numerical setups for the uncoated and coated cases are schematised in figures 1(a) and (b), respectively.

2.5. Mass gain calculation

In the FEM simulations, the normalised oxygen content ranges from 0.0–1.0. After initialisation of diffusion, the oxygen flux decays over time as the spatial distribution for the diffusion coefficient, D, decreases over the discretised materials domain(s) (section 2.3). For the mass gain calculation, the normalised increase in oxygen concentration at each time step is required to compare with experimental

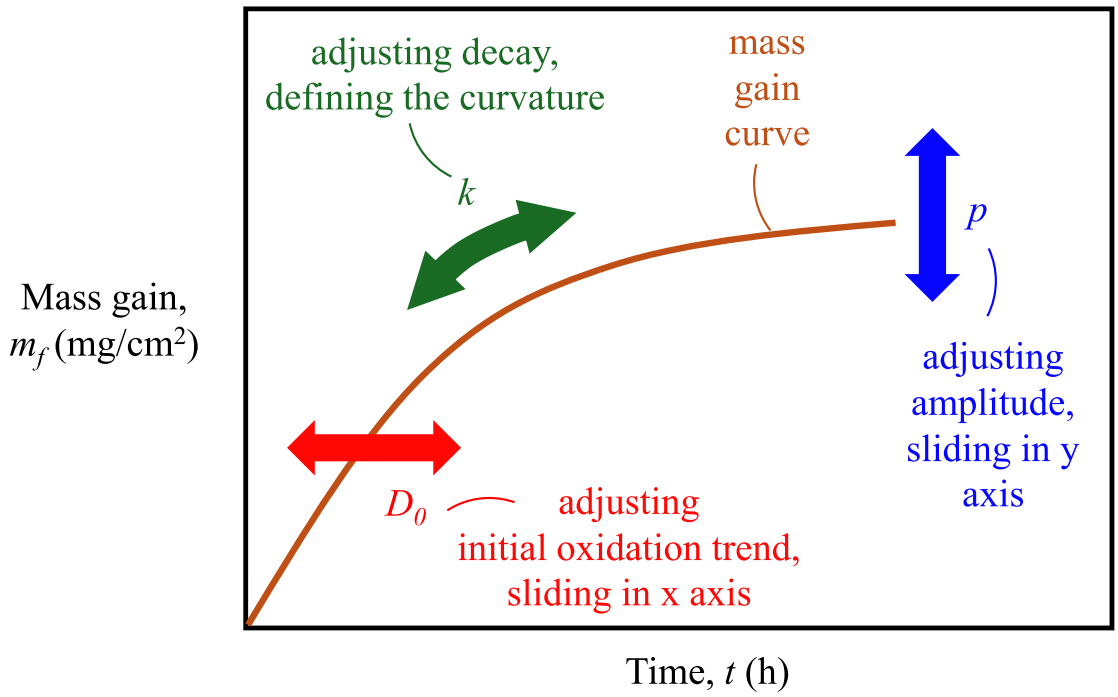


Figure 2. Numerical impact of the parameters D_0, k and p for the numerical mass gain calculation.

mass gain data. Numerically, the total normalised oxygen concentration is calculated as:

$$\dot{c}(t) = \int c(t)\,\mathrm{d}x, \tag{12}$$

where $\dot{c}(t)$ is the total normalised oxygen flux with the unit of [m] for the one-dimensional case. For calculating the numerical mass gain due to the oxygen addition, the following relation is proposed:

$$m_f(t) = \dot{c}(t)\,\rho_m p, \tag{13}$$

where $m_f(t)$ is the calculated mass gain data for time t using FEM, ρ_m is the density of the material, and p is the molar mass fraction of the oxygen in the oxide. (13) represents a similar mass gain formulation introduced by Vache *et al* for titanium alloy oxidation [31]. When applying (13), the variation in ρ_m is found to be negligible, as the mass gain resulting from oxidation can be neglected relative to the total mass of the sample. In the finite element model, the characteristic parameters D_0, k and p are calibrated in order to obtain a parabolic oxidation trend that compares well with the experimental data. The effect of these three parameters on the mass gain curve is demonstrated in figure 2. First, the parameter D_0 sets the initial oxidation speed that adjusts the initial slope of the mass gain curve. Second, the parameter k adjusts the curvature of that curve to capture the trend of the experimental mass gain data points. Third, the mass fraction parameter p amplifies the curve in the y direction to obtain good agreement with experimental data.

2.6. Numerical procedure

In this paper, a one-dimensional finite element domain with 5000 elements is considered. The coating thickness is chosen to be $L_c \approx 2.5\,\mu$m as in [12], and substrate thickness is assumed to be $L_s = 20\,L_c$. A degree 1 continuous Galerkin (CG1) finite element is used. With a time step of $\Delta t = 0.25$ h, transient simulations are performed for the final time of $T = 50$ h, then compared with the experimental data. Mesh- and time-step-dependent studies are presented in appendix B. For the coated oxidation cases, diffusion domains are marked with mesh tags and the corresponding diffusion coefficients, D_s, are imposed along with related parameters, D_0 and k, for each medium. The interface between these two media does not move, which may be a limitation of the proposed numerical framework. After calculating $\dot{c}$ for the corresponding test case, the resulting mass gain curve is amplified with p to fit the experimental mass gain data.

3. Results and discussion

In this section, the test cases to model oxidation kinetics of the uncoated and coated TE materials are presented. The modelling results are compared with the experimental data reported in [7, 12], and extrapolation case studies are performed for predicting the long-term mass gain due to the oxidation and coating thickness effect on the oxide scale formation.

3.1. Mass gain

Figure 3 shows the experimental and numerically modelled mass gain of the uncoated and CrSi-coated N-type and P-type HH materials during oxidation, respectively. The modelling of mass gain is initially performed for uncoated and coated N-type half-Heusler thermoelectric materials. The density of N-type material is measured to be $\rho_{m,\mathrm{N}} = 6.021\ 464 \times 10^{-8}$ mg $\mu\mathrm{m}^{-3}$. Firstly, the optimisation algorithm is run to calibrate D_0, k and p values for the uncoated case, and the numerical mass gain is calculated using (13). The optimiser returns $D_0 = 3 \times 10^{-5} \mu\mathrm{m}^2\ \mathrm{s}^{-1}$, $k = 0.005$ and $p = 0.43$ to fit the experimental data well. To verify the experimental mass gain data for the coated N-type case, the determined substrate parameters are used to calibrate the diffusion parameters of the coating material (CrSi) domain. This yields $D_0 = 2 \times 10^{-7} \mu\mathrm{m}^2\ \mathrm{s}^{-1}$, $k = 0.003$, and $p = 0.60$ for the coating material, in agreement with the experimental data.

After calculating the calibrated diffusion parameters for the N-type case, the same procedure to calculate the corresponding parameters is repeated for the P-type case. The density of P-type material is measured to be $\rho_{m,\mathrm{P}} = 6.589\ 692 \times 10^{-8}$ mg $\mu\mathrm{m}^{-3}$. Initially, the optimal parameters for the uncoated P-type substrate are computed, yielding $D_0 = 9 \times 10^{-6} \mu\mathrm{m}^2\ \mathrm{s}^{-1}$, $k = 0.015$ and $p = 0.34$. For the coated P-type case, the optimal diffusion parameters of the coating material obtained from the N-type calculations are used, since the same protective coating is used for the oxidation experiments. Using these parameters, comparison between the numerical and experimental mass gain curves for the uncoated and coated materials is plotted for 50 h and shown in figure 3.

Experimentally, the higher mass gain observed for the N-type material (figure 3(a)) compared to the P-type (figure 3(b)). These findings can be verified using the diffusivity observations from the calibrated model parameters: the N-type material consistently exhibits a higher diffusion coefficient than the P-type material over the entire time range. The faster diffusion rates of N-type material ($D_0 = 3 \times 10^{-5} \mu\mathrm{m}^2\ \mathrm{s}^{-1}$, $k = 0.005$) compared to the slower oxidation rates observed for the P-type material ($D_0 = 9 \times 10^{-6} \mu\mathrm{m}^2\ \mathrm{s}^{-1}$, $k = 0.015$) can be attributed to their different chemical compositions, as detailed in [7].

In both material systems, the uncoated samples exhibit significantly higher mass gain than the coated samples. The optimal diffusion coefficient for the CrSi material ($D_0 = 2 \times 10^{-7} \mu\mathrm{m}^2\ \mathrm{s}^{-1}$, $k = 0.003$) is found to be ≈ 150 and ≈ 45 times lower than that for the N- and P-type, respectively. These numerical findings confirm the barrier effect of the CrSi coating observed in the experimental study, as the protective coating limits inward oxygen diffusion and suppresses outward diffusion of high-affinity-to-oxygen elements such as Zr, Ti, and Sn, thereby lowering the overall mass gain [12].

The optimised oxygen molar mass fraction values for all oxidation cases are presented in figure 4. The N-type sample exhibits a higher oxygen molar mass fraction ($p = 0.43$) compared to the P-type ($p = 0.34$), which correlates well with its greater mass gain (figure 4) and higher diffusion coefficient (figure 5). However, the coated samples exhibit a more complex behaviour. While the coated P-type sample exhibits a significantly reduced oxygen molar mass fraction ($p = 0.15$), the coated N-type sample shows a high oxygen molar mass fraction ($p = 0.60$). This inconsistency can be explained by the combined effects of substrate-driven oxidation mechanisms and coating quality. Although the CrSi coating significantly reduces the overall diffusion coefficient and mass gain for the N-type sample, the relatively high oxygen mass fraction suggests that the oxygen that penetrates the coating is more effectively retained within the oxide scale. This may be related to oxygen diffusion through micro-defects, grain boundaries, or local imperfections in the coating, leading to localised but intense oxidation that results in a higher effective oxygen incorporation (higher mass fraction) despite the overall lower oxidation rate [12]. If the CrSi coating on the N-type sample contains more diffusion pathways than that on the P-type sample, it would allow localised oxygen penetration, increasing the oxygen mass fraction without necessarily leading to a proportionally large mass gain.

3.2. Diffusion coefficients

It is worth revealing the long term trends of the optimal diffusion coefficients found in section 3.1. Figure 5 shows the time-dependent evolution of the effective diffusion coefficients for 1000 h in $\log_{10}$

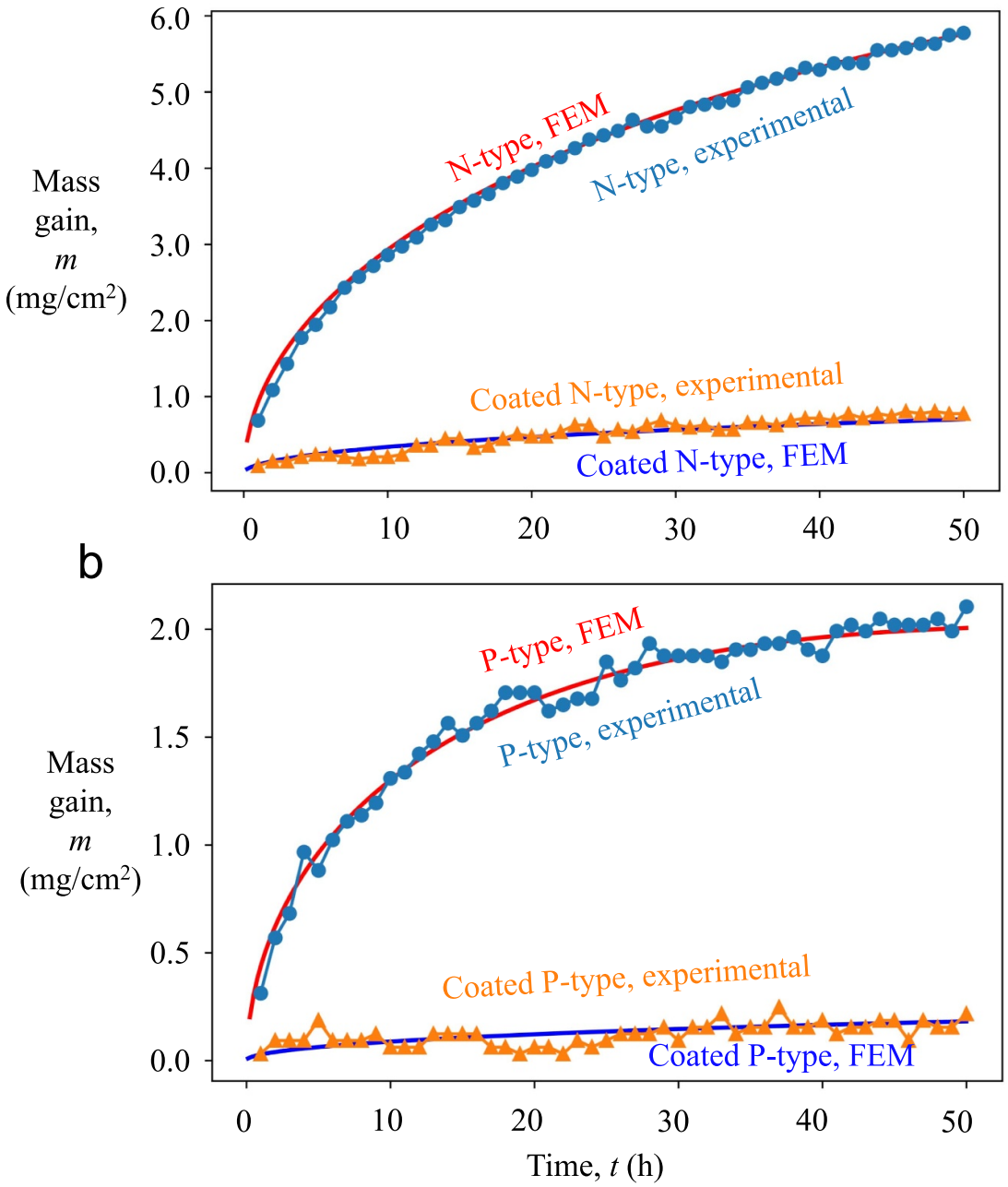


Figure 3. Mass gain profiles for (a) N-type and (b) P-type materials with coated and uncoated cases. The continuous lines represent the FEM results, and the circle and triangle markers denote experimental mass-gain data for the uncoated and coated cases, respectively.

scale, revealing a clear distinction between the diffusion behaviour of the uncoated thermoelectric substrates and that of the protective coating.

For both N-type and P-type materials, the diffusion coefficients decrease gradually over time, indicating a transition from an initial rapid oxidation to a more diffusion-limited regime. The degree of decrement in diffusion coefficient differs for each substrate as they have different decay rates (0.005 for the N-type and 0.015 for the P-type). From the numerical perspective, the diffusion coefficient of CrSi coating is initially lower than that of both N-type and P-type substrates, confirming the strong barrier effect of the coating against oxygen transport. However, as oxidation progresses, the diffusion coefficient of the coating decreases at a slower rate ($k = 0.003$) than that of the P-type material (0.015), and it exceeds that of the P-type after approximately 316 h (figure 5). This behaviour suggests that, while the coating effectively suppresses initial oxygen diffusion, the subsequent oxidation process is driven by oxide-layer

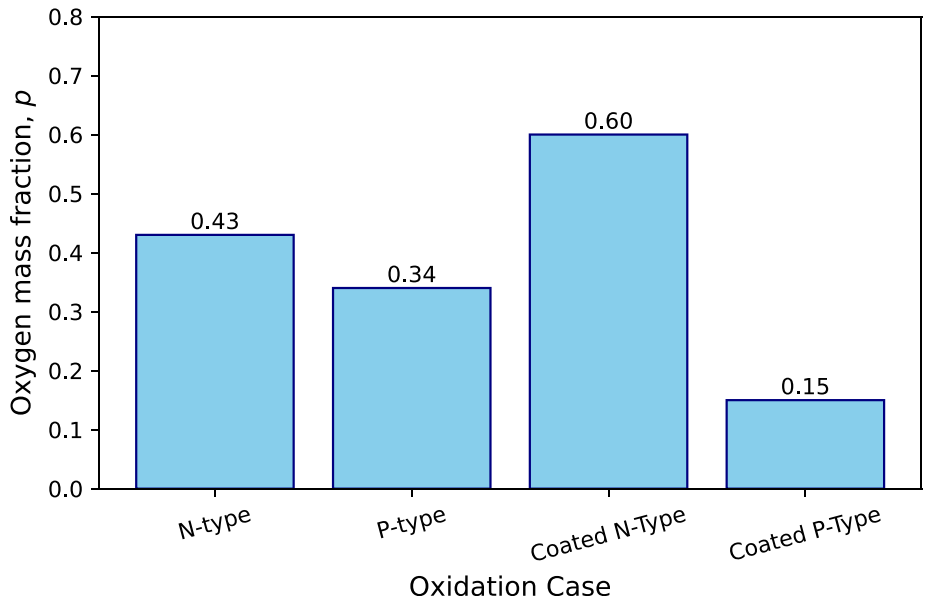


Figure 4. Numerically calculated optimal oxygen molar mass fractions for each oxidation case.

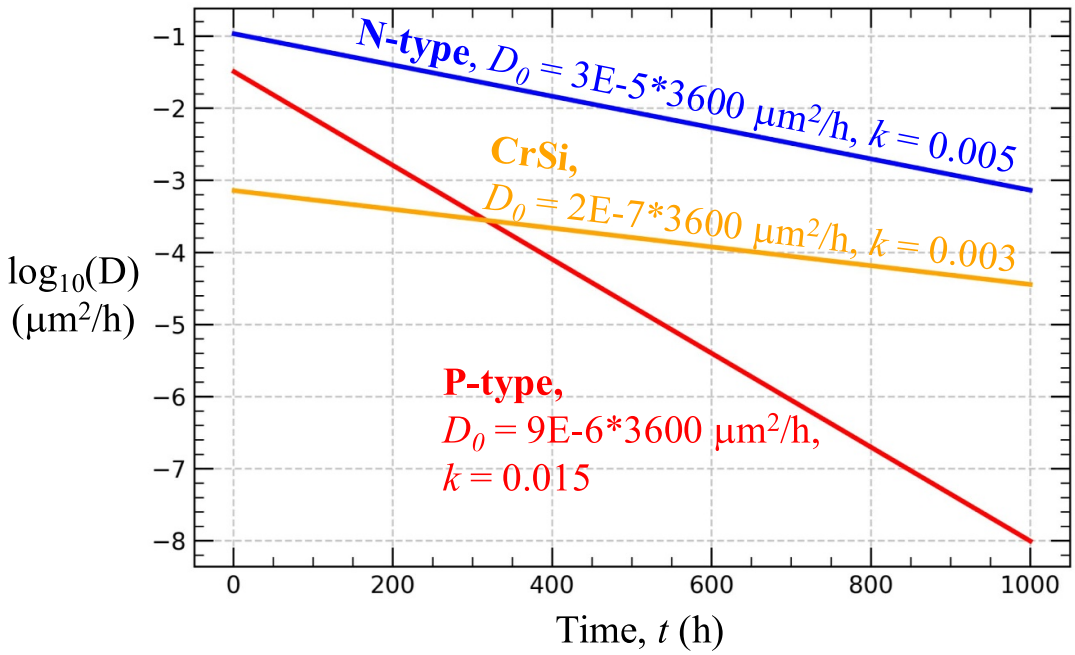


Figure 5. $\log_{10}(D)$-time plots for the numerically found optimal diffusion coefficients and decay rates for N-type, P-type and CrSi materials.

growth on the coating/material surface. The low diffusivity of oxygen can also be attributed to the formation of a top oxide layer formed on the coating and substrate materials during thermal treatment, which is more than 100 times denser than the bulk material [32]. However, although the protectivity of the oxide scale formed on the P-type material is effective for a long exposure to aggressive oxygen at elevated temperatures, it should be noted that the post-oxidation products being formed on the uncoated material surface significantly alter the thermoelectric performance due to the change in chemical composition of the surface.

3.3. Growth of oxide scale

Using the calibrated diffusion parameters for the coated TE materials in section 3.1 and the numerical framework's tunability, oxide scale growth can be modelled. To begin with, an experimental investigation of oxide scale growth is performed on both N-type and P-type materials coated with CrSi. Figure 6 shows the back-scattered electron microscope (BEI) images of the cross-sections of CrSi-coated N-type and P-type materials after 50 h of oxidation. In both cases, a continuous oxide layer forms on the coating surface, thereby reducing oxidation kinetics. However, the oxide scale formed on the coated N-type material appears thicker ($\approx 0.67\,\mu$m) compared to that on the coated P-type material ($\approx 0.44\,\mu$m), suggesting that the CrSi coating is more efficient on the P-type substrate. This can be attributed to either the quality of the deposited coating, as discussed in section 3.1, or to the effect of the substrate material on the coating's protective performance. Further, the observed differences in oxide scale thickness support the oxygen mass fraction results (figure 4), where the coated N-type sample exhibits a considerably higher value due to its continued oxygen uptake, which promotes further oxide scale growth during oxidation.

For numerically calculating the oxide scale using FEM, a concentration threshold, c_{th}, is set to a value between 0.0 and 1.0 to advance the oxygen diffusion front. This threshold defines the oxide scale being formed across the oxygen-affected zone. If the normalised oxygen concentration (c) is greater than or equal to the c_{th} for a given thickness x, at time (t), then x is specified as the oxide scale thickness, $d(t)$. The oxide scale formation, $d(t)$, increases parabolically as $t \longrightarrow \infty$. The visual representation for the oxide scale calculation is shown in figure 7.

The oxide scales from SEM images (figure 6) are analysed to determine the coating material and oxide scale thicknesses, and c_{th} is calibrated to match the experimental data. For this, the concentration threshold is found to be $c_{\text{th}} = 0.05$, giving $d(50) \approx 0.51\mu$m for the 50 h of oxidation. This procedure for calculating oxide scale thickness can also be used to conduct extrapolation studies to simulate oxide scale growth, as presented in section 3.4.

3.4. Extrapolation

At this point, the calibrated model parameters enable extrapolation studies to assess the long-term performance of the TE materials. Therefore, two extrapolation test cases are presented: one to assess oxide scale formation over 1000 h, and the other to investigate the influence of varying coating thickness on mass gain over 100 h.

To start with, the evolution of oxide scale thickness for the CrSi coating as a function of time is presented in figure 8. The growth follows a parabolic trend, confirming diffusion-controlled mechanisms during thermal exposure. The oxide layer formed on the top surface of the coating increasingly limits oxygen transport, leading to a gradual reduction in the growth rate and indicating the formation of a stable, protective scale. Based on the modelling results, the oxide thickness reaches approximately 1.75 μm after 1000 h of oxidation, showing the protective capability of CrSi coating over an extended period. Such behaviour is consistent with the lower mass gain increase over time for the coated cases (figure 3), as well as the reduced diffusion coefficients and improved oxidation kinetics observed in figure 5. This predictive insight into long-term coating performance is highly valuable, enabling the design of a TE module with oxidation-protected TE materials. In addition, maintaining oxide thickness within a limited range (on the order of a few μm) is critical to avoid negative effects (due to chemical composition alteration) on thermal and electrical transport across the TE power generator.

As a second extrapolation study, the influence of CrSi coating thickness on mass gain behaviour is predicted for coated N-type and P-type TE materials over 100 h. The resulting mass gain curves are plotted in figure 9. In both material systems, increasing the coating thickness leads to a systematic reduction in mass gain. For the N-type material (figure 9(a), the thinnest coating (0.05 μm) results in the highest mass gain (1.09 mg cm^{-2}), indicating insufficient resistance to oxygen diffusion. Here, oxygen is more likely to rapidly reach the N-type material by passing through the thin coating layer, leading to continuous oxidation there. As the coating thickness increases to 0.1 μm and 0.25 μm, the mass gain decreases significantly, indicating improved barrier properties. The thickest coating, 2.5 μm, provides the highest level of protection, resulting in 75% reduction in the mass gain (0.25 mg cm^{-2}) compared to the 0.05 μm of coating thickness over the specified oxidation duration. This behaviour confirms that increasing coating thickness effectively suppresses oxidation by extending the diffusion path for oxygen. However, the rate of improvement diminishes at higher thicknesses, suggesting that once a sufficiently protective barrier is formed, further increases in thickness yield only marginal benefits and are likely not necessary.

A similar overall trend in the relationship between mass gain and coating thickness was also observed for the coated P-type material (figure 9(b)). However, compared to the N-type case (figure 9(a)), the

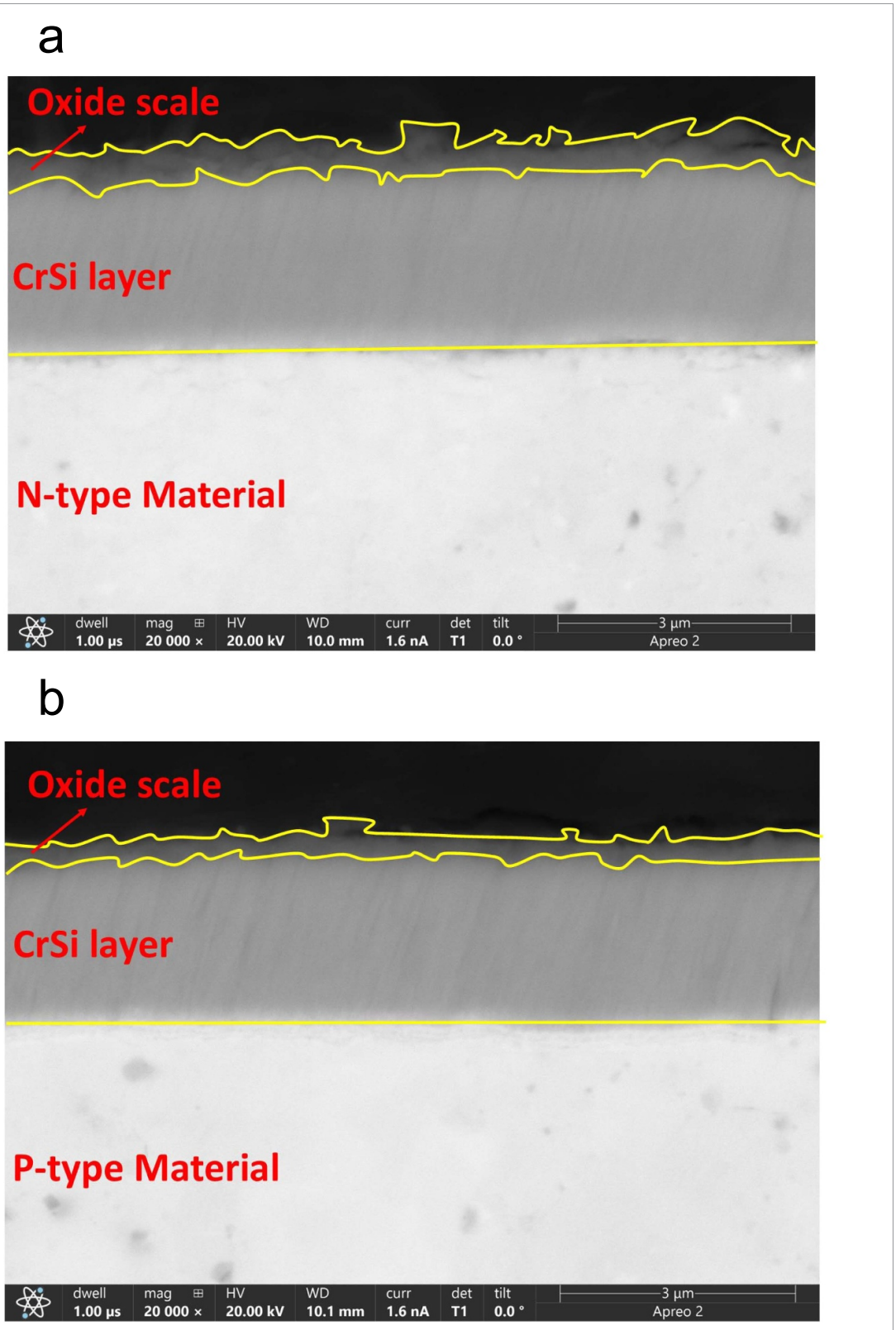


Figure 6. BEI images for (a) coated N-type and (b) coated P-type after 50 h of oxidation. Technical details regarding the experimental work are given in [7, 12].

P-type material consistently exhibits lower mass gain values for all coating thicknesses, indicating that the P-type substrate has a lower oxidation tendency. For example, 22% less mass gain (0.86 mg cm^{-2}) is observed for the P-type coated case compared to the N-type coated case, considering the coating thickness of 0.05 μm. However, as the coating thickness increases, the change in mass gain trends between N-type and P-type materials becomes relatively small. For a coating thickness of 2.5 μm, the P-type coated case yields a mass gain of 0.24 mg cm^{-2}, which is only 4% less than that of the N-type material. This is

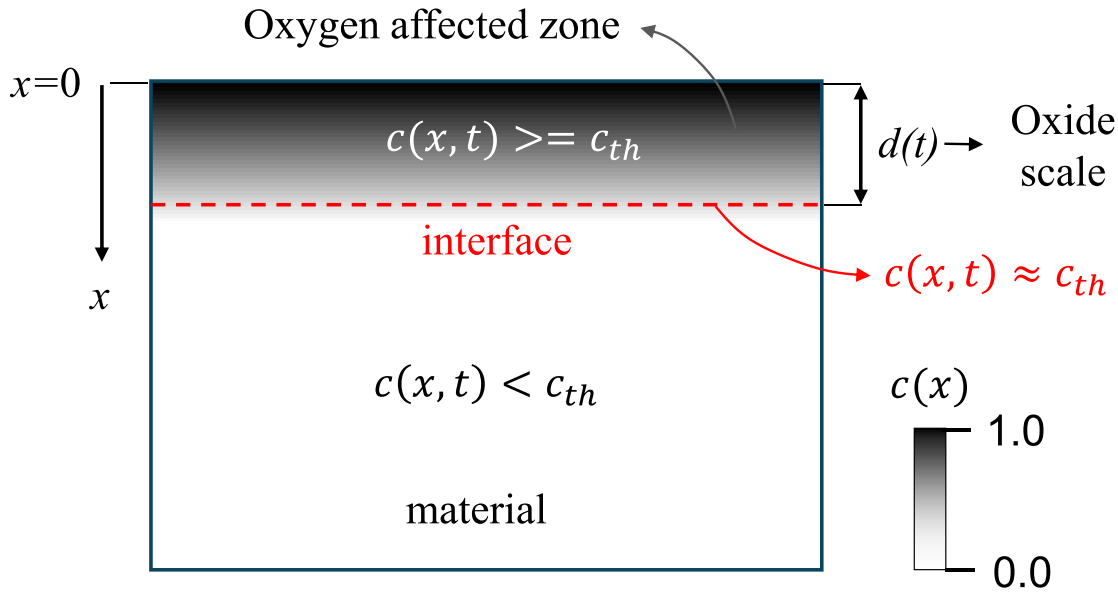


Figure 7. Schematic representation for the oxide scale calculation.

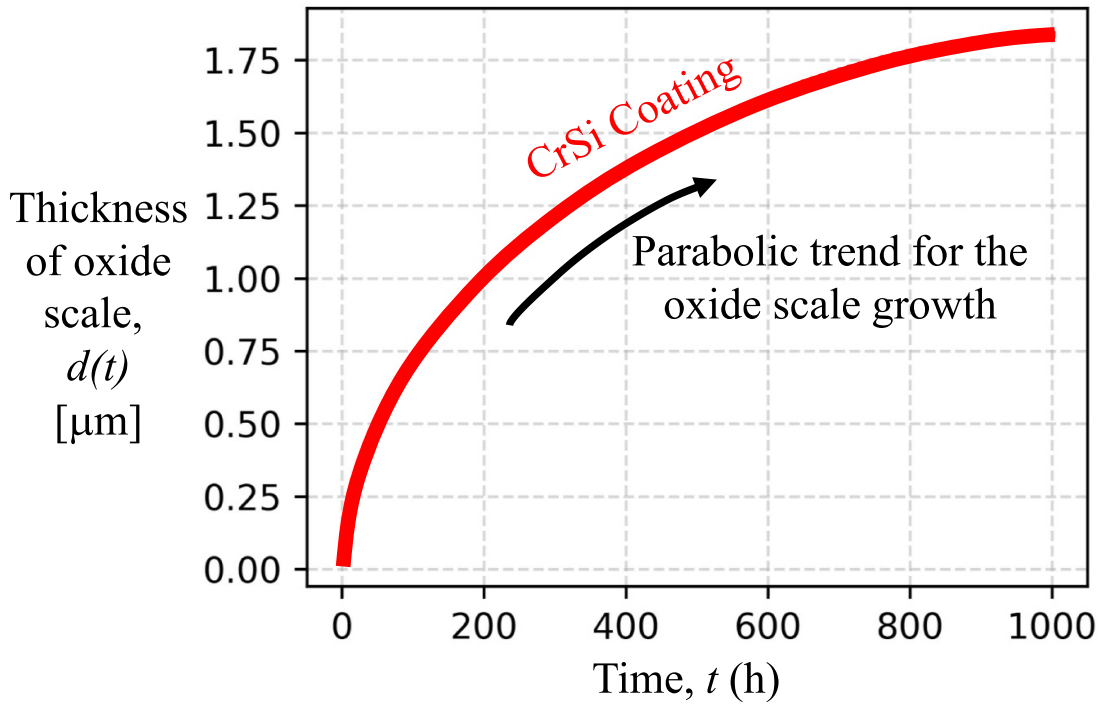


Figure 8. Oxide scale thickness evolution over 1000 h for CrSi coating.

not surprising because the advancing oxygen diffusion front sweeps the same spatial region for increased coating thicknesses in both material systems, yielding similar mass gain profiles over 100 h. This is consistent with the experimental and modelled mass gain results shown in figure 3 for 50 h. Overall, these extrapolation findings emphasise the importance of designing the coating thickness according to the substrate composition to achieve optimal thermoelectric performance.

3.5. Limitations

The model parameters are calibrated on 50 h mass-gain data, so the long-term results are extrapolations that remain to be validated by long-duration oxidation tests. Because the diffusivity decays exponentially, the cumulative diffusivity approaches D_0/k, and mass gain and scale thickness level off at long times.

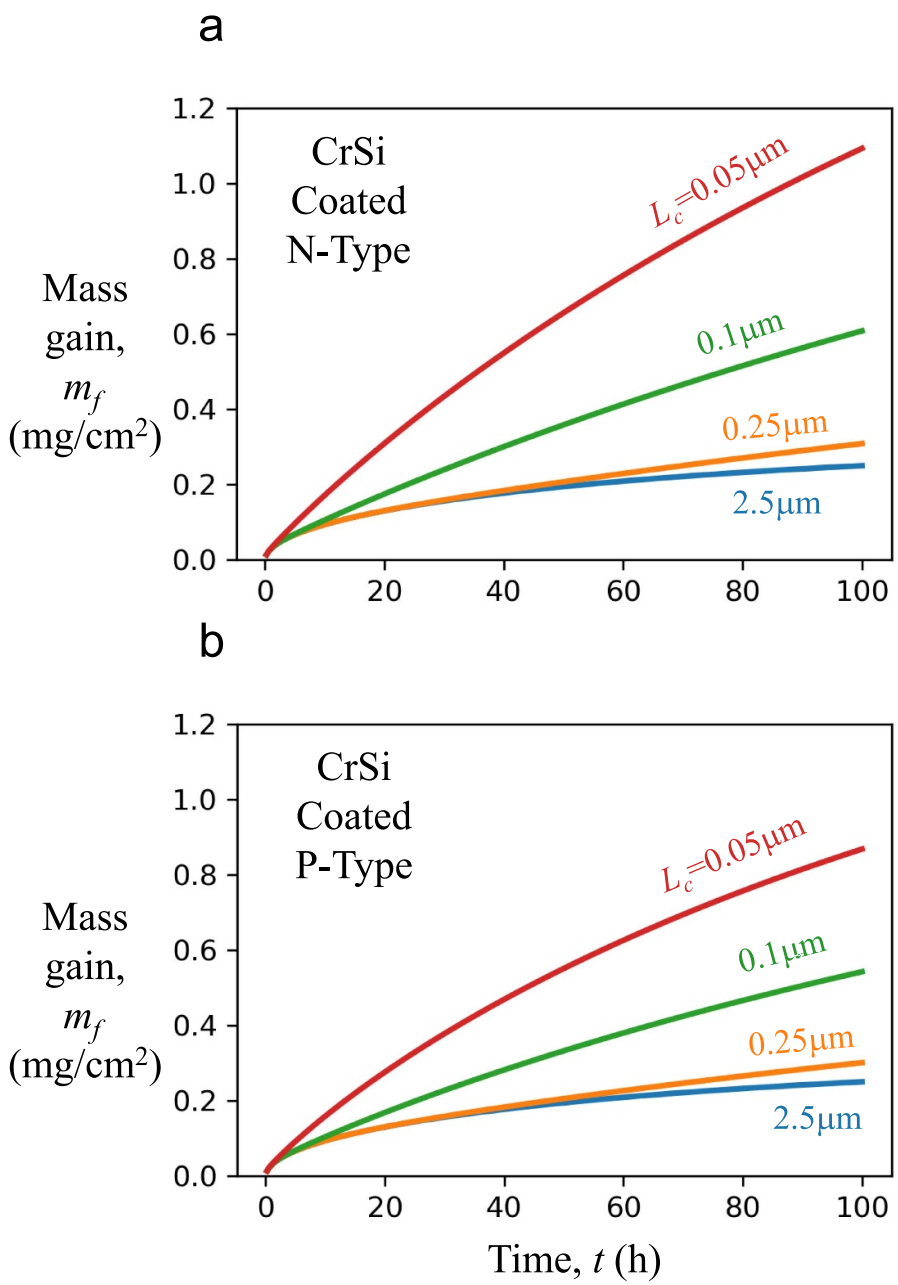


Figure 9. Mass gain profiles for different coating thickness values considering (a) Coated N-type and (b) coated P-type cases for the duration of 100 hours.

The long-term predictions are therefore sensitive to the calibrated decay rate k. In addition, the coating–substrate interface is fixed, whereas moving-interface models such as EKINOX and PyTiOx account for scale growth explicitly.

4. Conclusions

In this paper, for the first time, the oxidation behaviour of N-type (Zr,Ti)Ni(Sn,Sb) and P-type (Zr,Ti)Co(Sn,Sb) HH materials at elevated temperatures is numerically studied using finite element-based oxygen diffusion modelling. After calibration, the model reproduces the measured mass gain, gives an oxide scale thickness within the measured range, and enables extrapolation of long-term behaviour. In addition, the long-term thermal stability of the CrSi coating layer at 500 °C is incorporated into the oxidation modelling. Based on the key findings, the study can be concluded as follows:

1. In both materials, the numerical results for the uncoated cases exhibit significantly higher mass gain than the coated samples, as for the experimental findings, indicating severe oxidation of uncoated materials and effective oxidation-protective performance of the CrSi coating layer.
2. The time-dependent diffusion coefficients of N-type and P-type materials decrease gradually over time. However, the diffusion coefficient of the coating decreases more slowly than that of the P-type material.
3. The coated N-type sample shows the highest oxygen molar mass fraction among all samples as a result of diffusion of oxygen through micro-defects, grain boundaries, or local imperfections in the coating. The localised but intense oxidation results in a higher effective oxygen incorporation despite the overall lower oxidation rate.
4. The oxide layer formed on the top surface of the CrSi coating during oxidation limits the inward diffusion of oxygen, providing a gradual reduction in the growth rate of protective oxide scale. Based on extrapolation of the numerical model results, the top-oxide scale thickness reaches approximately 1.75 μm after 1000 h of oxidation, indicating the protective capability of the CrSi coating over an extended period.
5. Increasing the coating thickness leads to a systematic reduction in mass gain in both materials. The thinnest coating (0.05 μm) results in the highest mass gain, indicating insufficient resistance to oxygen diffusion. The numerical study reveals that although the thickest coating, 2.5 μm, provides the highest level of protection, the rate of improvement diminishes at higher thicknesses, suggesting that further increases in thickness are not necessary, as a sufficient protective layer is formed.

Future work will extend the present diffusion-based oxidation modelling to other thermoelectric material systems and protective coatings, enabling an understanding of oxidation mechanisms across different compositions. Such an approach will provide a powerful predictive tool for estimating long-term behaviour and lifetime of TE materials operating at high temperatures, supporting the reliable design of TE modules for energy harvesting technologies.

Acknowledgments

Ekrem Ekici gratefully acknowledges funding for his postgraduate studies from Türkiye's Ministry of National Education. Mikdat Gurtaran would like to acknowledge Prof. Hanshan Dong, Dr Xiaoying Li and Dr Zhenxue Zhang for their supervision during his research work carried out at the University of Birmingham (UK).

Data availability statement

The data that support the findings of this study are openly available at the following URL/DOI:. https://github.com/ekremekc/oxidation [34].

Funding

Funding information is not available.

Author contributions

Ekrem Ekici 0000-0002-5885-790X
Conceptualization (equal), Data curation (equal), Investigation (equal), Methodology (equal), Software (equal), Validation (equal), Visualization (equal), Writing – original draft (equal)

Mikdat Gurtaran 0000-0002-8953-7458
Data curation (equal), Formal analysis (equal), Investigation (equal), Methodology (equal), Project administration (equal), Supervision (equal), Visualization (equal), Writing – review & editing (equal)

Appendix A. Numerical verification of the code

For transient verification, we design a 1D transient test case with Dirichlet BCs. We consider a 1D domain with length $L = 50.0$, and set the initial concentration of the domain to 1, $u(x,0) = 1$. When $t > 0$, we impose $\phi(0,t) = \phi(L,t) = 0.0$ for the both ends. The analytical solution for $u(x,t)$ becomes (section 10.5 in [33]):

$$u(x,t) = \frac{80}{\pi} \sum_{n=1,3,5,\ldots}^{N} \frac{1}{n} e^{-n^2\pi^2\alpha^2 t/2500} \sin\frac{n\pi x}{50}. \tag{14}$$

We present the transient behaviour of the domain for $t = [20, 50, 150, 300]$ in figure 10. The results of the analytical and numerical solutions agree well.

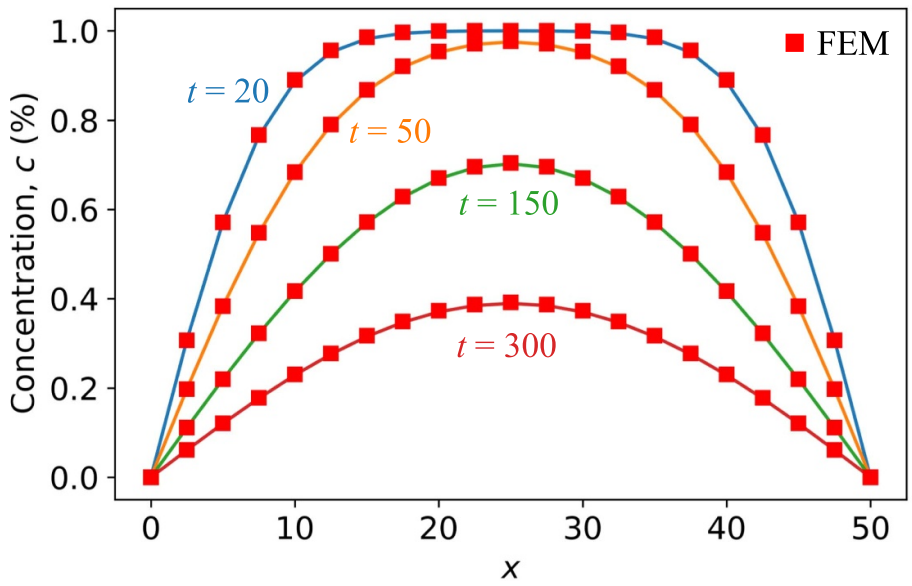


Figure 10. Comparison between analytical solution and FEM simulation of 1D transient case with Dirichlet BCs for both ends. The red square markers denote the FEM results, and the continuous lines denote the analytical solutions.

Appendix B. Mesh and timestep convergence

To assess mesh and time-step independence of the solution to the finite element system, we conduct convergence studies for both. We use $D_0 = 3 \times 10^{-5} \mu m^2\ s^{-1}$ and $k = 0.005$ in this section. For the number of finite elements in one-dimensional numerical grid, more than 5000 elements yield negligible influence on the total mass gain at $t = 50$ h as shown in figure 11(a). Next, we span the time steps, Δt s from $\Delta t = 5$h to $\Delta t = 0.125$ h using 5000 finite elements. We find minimal changes for the calculated total mass gain at $t = 50$ h using $\Delta t = 0.25$ h, as shown by the $\log(m_f)$-$\log(\Delta t)$ plot in figure 11(b).

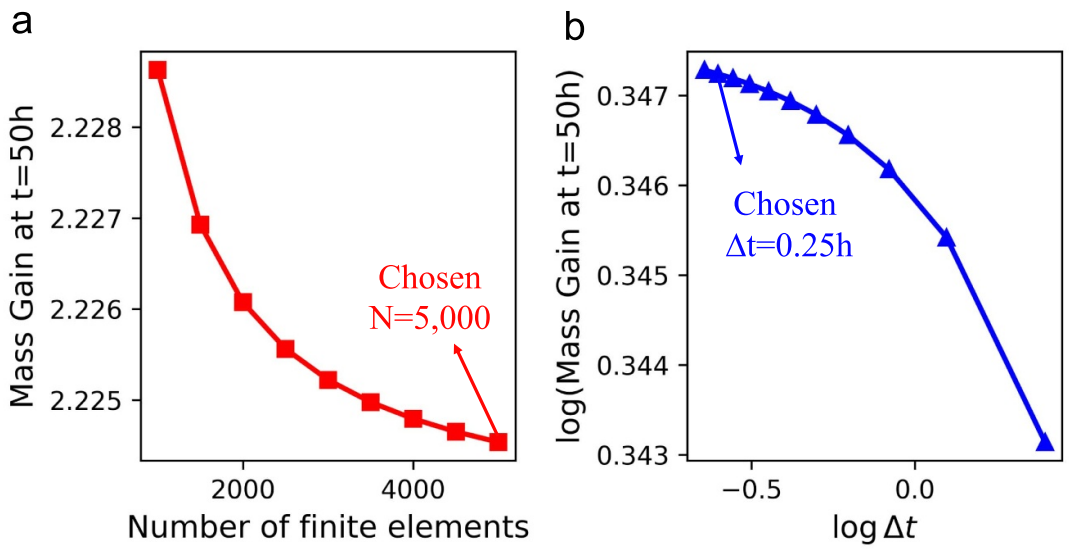


Figure 11. (a) Mesh and (b) timestep convergence studies with the chosen number of finite elements and timestep for 1D calculations in this paper.

References

[1] Bos J W G and Downie R A 2014 Half-Heusler thermoelectrics: a complex class of materials *J. Phys.: Condens. Matter* **26** 433201
[2] Li W, Ghosh S, Liu N and Poudel B 2024 Half-Heusler thermoelectrics: advances from materials fundamental to device engineering *Joule* **8** 1274–311
[3] Rogl G and Rogl P F 2023 Development of thermoelectric half-Heusler alloys over the past 25 years *Crystals* **13** 1152
[4] Wang Q, Zhao Y, Fang T, Xi J and Yang J 2026 Temperature-dependent band renormalization in half-Heusler MNiSn and MCoSb (M = Ti, Zr, Hf) *Appl. Phys. Lett.* **128** 10
[5] Li S, Bao X, Yin L, Ye X, Mao J and Zhang Q 2024 Temperature-dependent band renormalization in half-Heusler MNiSn and MCoSb (M = Ti, Zr, Hf) *Acta Mater.* **271** 119896
[6] Szybist J, Davis S, Thomas J and Kaul B C 2018 Performance of a half-Heusler thermoelectric generator for automotive application *Tech. Rep. SAE Technical paper*
[7] Gurtaran M, Zhang Z, Li X and Dong H 2024 Cyclic oxidation behaviour of N-type (Zr,Ti)Ni(Sn,Sb) and P-type (Zr,Ti)Co(Sn,Sb) thermoelectric materials *J. Mater. Res. Technol.* **30** 7476–84
[8] Wang L, Song Q, Gu J, Wang C, Bai S and Chen L 2023 High temperature oxidation behavior of ZrNiSn-based half-Heusler thermoelectric material *Corros. Sci.* **225** 111606
[9] Gu J, Wang L, Song Q, Wang C, Xia X, Liao J, Sun Y Y, Chen L and Bai S 2023 High-temperature oxidation mechanism of ZrCoSb-based half-Heusler thermoelectric compounds *J. Mater. Sci. Technol.* **148** 242–9
[10] Appel O, Breuer G, Cohen S, Beeri O, Kyratsi T, Gelbstein Y and Zalkind S 2019 The initial stage in oxidation of ZrNiSn (half-Heusler) alloy by oxygen *Materials* **12** 1509
[11] Berche A and Jund P 2018 Oxidation of half-Heusler NiTiSn materials: implications for thermoelectric applications *Intermetallics* **92** 62–71
[12] Gurtaran M, Zhang Z, Li X and Dong H 2024 Developing advanced CrSi coatings for combatting surface degradation of N-type (Zr,Ti)Ni(Sn,Sb) and P-type (Zr,Ti)Co(Sn,Sb) half Heusler thermoelectric materials *J. Mater. Res. Technol.* **32** 3288–301
[13] Gurtaran M, Zhang Z, Li X and Dong H 2025 Protection of n-type (Ni,Fe)TiSb half-Heusler materials against static and cyclic oxidation using a Si-doped Cr coating *ACS Omega* **10** 50666–78
[14] Birks N, Meier G H and Pettit F S 2006 *Introduction to the High Temperature Oxidation of Metals* (Cambridge University Press)
[15] Wagner C 1933 Beitrag zur Theorie des Anlaufvorgangs *Z. Für Phys. Chem.* **21** 25–41
[16] Wagner C 1952 Theoretical Analysis of the Diffusion Processes Determining the Oxidation Rate of Alloys *J. Electrochem. Soc.* **99** 369–80
[17] Stringer J 1960 The oxidation of titanium in oxygen at high temperatures *Acta Metall.* **8** 758–66
[18] Kofstad P 1967 High-temperature oxidation of titanium *J. Less Common Met.* **12** 449–64
[19] Kitashima T, Liu L J and Murakami H 2013 Numerical Analysis of Oxygen Transport in Alpha Titanium during Isothermal Oxidation *J. Electrochem. Soc.* **160** C441
[20] Kitashima T and Kawamura T 2016 Prediction of oxidation behavior of near-α titanium alloys *Scr. Mater.* **124** 56–58
[21] Bertrand N, Desgranges C, Nastar M, Girardin G, Poquillon D and Monceau D 2008 Chemical evolution in the substrate due to oxidation: a numerical model with explicit treatment of vacancy fluxes *Materials Science Forum* vol 595 (Trans Tech Publ) pp 463–72
[22] Mazères B, Desgranges C, Toffolon-Masclet C and Monceau D 2016 Experimental study and numerical simulation of high temperature (1100–1250 °C) oxidation of prior-oxidized zirconium alloy *Corros. Sci.* **103** 10–19
[23] Bataillou L, Desgranges C, Martinelli L and Monceau D 2018 Modelling of the effect of grain boundary diffusion on the oxidation of Ni-Cr alloys at high temperature *Corros. Sci.* **136** 148–60
[24] Ciszak C, Monceau D and Desgranges C 2020 Modelling the high temperature oxidation of titanium alloys: Development of a new numerical tool PyTiOx *Corros. Sci.* **176** 109005

[25] Barrata I A, Dean J P, Dokken J S, Habera M, Hale J, Richardson C, Rognes M E, Scroggs M W, Sime N and Wells G N 2023 DOLFINx: the next generation FEniCS problem solving environment
[26] Alnæs M S 2012 UFL: a finite element form language *Automated Solution of Differential Equations by the Finite Element Method: the Fenics Book* (Springer) pp 303–38
[27] Logg A, Ølgaard K B, Rognes M E and Wells G N 2012 Automated solution of differential equations by the finite element method *The FEniCS Book* (Springer) (https://doi.org/10.1007/978-3-642-23099-8) pp 227–38
[28] Balay S *et al* 2020 (PETSc Users Manual Rev. 3.13)
[29] Dalcin L D, Paz R R, Kler P A and Cosimo A 2011 Parallel distributed computing using Python *Adv. Water Resour.* **34** 1124–39
[30] Gucci F, D'Isanto F, Zhang R, Reece M J, Smeacetto F and Salvo M 2019 Oxidation protective hybrid coating for thermoelectric materials *Materials* **12** 573
[31] Vaché N, Cadoret Y, Dod B and Monceau D 2021 Modeling the oxidation kinetics of titanium alloys: review, method and application to Ti-64 and Ti-6242s alloys *Corros. Sci.* **178** 109041
[32] Godlewski J, Lambertin M, Gros J, Wadier J and Weidinger H 1991 Raman spectroscopy study of the tetragonal-to-monoclinic transition in zirconium oxide scales and determination of overall oxygen diffusion by nuclear microanalysis of o *Zirconium in the Nuclear Industry: 9th Int. Symp.* (ASTM International) pp 416–36
[33] Boyce W E, DiPrima R C and Meade D B 2021 *Elementary Differential Equations and Boundary Value Problems* 12th edn (Wiley)
[34] Ekici E and Gurtaran M 2026 Oxygen diffusion in thermoelectric materials *Github* (available at: https://github.com/ekremekc/oxidation)